Journal of Colloid and Interface Science 496 (2017) 211–221

Contents lists available at ScienceDirect

Journal of Colloid and Interface Science

journal homepage: www.elsevier.com/locate/jcis

Regular Article

# Photochemical reactivity of apical oxygen in $KSr_2Nb_5O_{15}$ materials for environmental remediation under UV irradiation

Juan Matos [a,*], Silvania Lanfredi [b,*], Ricmary Montaña [a], Marcos A.L. Nobre [b], María C. Fernández de Córdoba [c], Conchi O. Ania [c,d]

[a] Biomaterials Department, Technological Development Unit (UDT), University of Concepcion, Av. Cordillera, 2634, Parque Industrial Coronel, Concepción, Chile
[b] São Paulo State University (UNESP), School of Technology and Sciences, Presidente Prudente, Laboratory of Composites and Ceramics Functional – LaCCeF, P.O Box 467, 19060-900, Brazil
[c] Instituto Nacional del Carbón (INCAR, CSIC), 33011 Oviedo, Spain
[d] CEMHTI UPR 3079, CNRS, Univ. Orléans, 45071 Orléans, France

## GRAPHICAL ABSTRACT

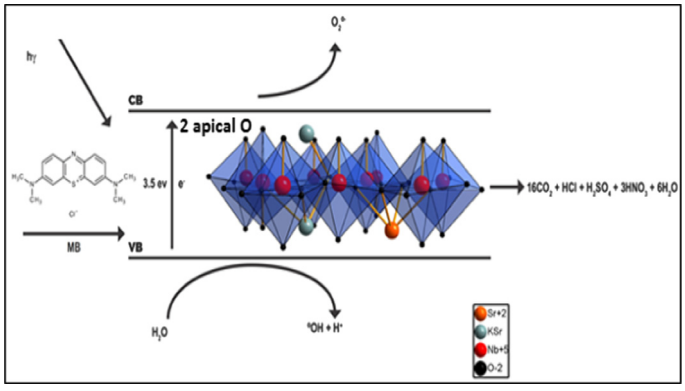


## ARTICLE INFO

*Article history:*
Received 2 December 2016
Revised 23 January 2017
Accepted 12 February 2017
Available online 14 February 2017

*Keywords:*
Photocatalysis
Niobate-based materials
Structural refinements
Methylene blue

## ABSTRACT

The photocatalytic activity of a series of novel $KSr_2Nb_5O_{15}$ materials was studied using the photooxidation of methylene blue as model reaction. The influence of the calcination time upon the crystalline structure and photoactivity was verified. Characterization was performed by XRD, SEM, FTIR, UV–Vis/DR, Helium picnometry, and $N_2$ and $CO_2$ adsorption-desorption isotherms. The diffraction line profile and the refinement of the structural parameters of $KSr_2Nb_5O_{15}$ were obtained from the XRD patterns by the Rietveld method. Data showed that samples were photoactive under UV irradiation, regardless the synthesis conditions. However, the calcination time had a clear influence upon the photocatalytic activity of the samples, being more efficient towards the degradation of the dye those obtained at a lower calcination time. Indeed, the sample calcined for 4 h showed up to 4 times higher photocatalytic activity than commercial $TiO_2$. Additionally, a correlation between the photocatalytic activity and the displacement of the Nb ion from the central position in the [$NbO_6$] octahedron was found. It is suggested that this fact causes an important polarization of the niobate structure. The apical oxygen in these samples is very reactive and can lead to the formation of superoxoradical anions ($O_2^{\cdot-}$) showing that $KSr_2Nb_5O_{15}$ can be potentially used in photocatalytic reactions under UV irradiation.



* Corresponding authors.
*E-mail addresses:* jmatoslale@gmail.com (J. Matos), silvania@fct.unesp.br (S. Lanfredi).

http://dx.doi.org/10.1016/j.jcis.2017.02.028
0021-9797/

## 1. Introduction

The development of more efficient processes for the remediation of polluted water remains one of the most important challenges of modern science and society nowadays [1]. Among different technologies, advanced oxidation processes (AOP's) based on heterogeneous photocatalysis have been extensively studied, due to the availability of a wide variety of efficient photocatalysts with excellent performance for the degradation of a number of pollutants. Although $TiO_2$ is considered the benchmark material in photocatalytic processes for water and air purification [2,3], this photocatalyst presents important limitations that prevent the large scale implementation of AOP's, mainly linked to a low absorption of sunlight (c.a. 6% solar spectra). For this reason, research on the development of more active and low-cost photocatalysts under solar irradiation is a widely investigated topic.

On the other hand, niobium is a particularly abundant element in Latin America, and it has been recently demonstrated that niobate-based materials are interesting candidates as photocatalysts in various applications due to the availability of precursor (i.e., low cost) and improved light absorption features -compared to titania- [4–6]. Niobate-based oxides are ferroelectric with a tetragonal tungsten bronze (TTB)-type structure, also considered a derivative of the classical perovskite structure described by the chemical formula $(A1)_2(A2)_4C4Nb_{10}O_{30}$ (where A1, A2, and C denote cations in different sites in the crystalline structure) [7,8]. The cation substitution in the interstices of the TTB structure allows modulating the physicochemical properties of the niobate-based oxides (i.e., optical, pyroelectric, electrical) [9]. Another important advantage of niobate-based oxides with a TTB structure-compared to $Nb_2O_5$-, is their high stability in aqueous solution [10,11], which makes them potential candidates to be used at the forefront of research and industrial applications [11]. As a few examples, niobate-based oxides have been reported to show activity in various catalytic processes: oxidative dehydrogenation of alkanes [12], oxidative coupling of methane [13], oxidation and ammoxidation of olefins [14], removal of nitrogen oxides in preventing air pollution [15], CO hydrogenation toward high hydrocarbons [16], hydrotreating reactions [17], organic synthesis by solid-acid assisted-catalysis [18] and water splitting [19]. More recently, our own studies have demonstrated the excellent catalytic (e.g., dry methane reforming and ethylene homologation reactions) and photocatalytic (e.g., degradation of red phenol) performance of Nb-based materials [20,21].

Considering this, the objective of this work was to explore the photocatalytic activity of $KSr_2Nb_5O_{15}$ materials under simulated solar light for the degradation of a dye (i.e., methylene blue). Methylene blue (MB) is a major representative of dyes largely used in textile industry, and thus discharged in textile effluents [22,23]. The literature on the degradation of dyes, and particularly methylene blue using AOP's is quite extense [24–31]. This molecule was chosen for the adsorption in the dark and for the photocatalytic tests because it shows interesting advantages in comparison to phenolic-based molecules such as rapid photodegradation [24], adsorption can be controlled by chemical affinity of the positive charged niobate-based materials [26], and the mechanism of photodegradation is very well-known [2].

To evaluate the impact of the photocatalyst' structure and composition on its photoactivity towards the degradation of the dye, photocatalytic degradation assays were carried out under UV irradiation on niobate-based photocatalysts obtained varying the calcination time (thus allowing to modulate different structural properties on the catalyst).

## 2. Experimental procedure

### 2.1. Synthesis

$KSr_2Nb_5O_{15}$ powders were prepared by the mechanical mixture of the metallic oxides and carbonates via high-energy ball milling (HEBM) [20,32]. The starting reagents were high purity $K_2CO_3$ (99.0% Reagen), $SrCO_3$ (99.0% Reagen), and hydrated niobium oxide, $Nb_2O_5{\cdot}4H_2O$, (CBMM-Brazil). The preparation was carried out using a HEBM type Attritor (Netzsch) with a milling chamber of zirconia (600 mL) with a cooling water circulation system. The mixture of the pristine reagents was carried out in isopropyl alcohol using stabilized zirconia balls of 1.2 mm in diameter (powder: ball weight ratio of 1:16). The mixture was stirred with a Molinex-type agitator shaft with eccentric radial disks that accelerated the grinding media, which gave an extra radial impulse during each rotation of the shaft with a motor of 1/3 hp. The milling was performed with a rate of 1200 rpm for 5 h. After milling, the solids were dried in a glove box with forced air flow at 100 °C (Fanen – model Orion 520). Single phase powders were obtained after calcination at 1100 °C for 4, 6, 8 and 12 h; the samples were denoted as KSrNb-4, KSrNb-6, KSrNb-8, and KSrNb-12, respectively. The calcination was carried out in a tube furnace under a constant oxygen flow of 300 mL/min. The powders were finally grinded in an agate mortar, and sieved using a 350-mesh minimum.

### 2.2. Characterization

Structural characterization of the prepared $KSr_2Nb_5O_{15}$ powders was carried out by X-ray diffraction (XRD) using a Shimadzu (model XRD-6000) diffractometer with Cu-K$\alpha$ radiation ($\lambda$ = 1.5418 Å) and a graphite monochromator. Measurements were carried out over an angular range of $5° \leq 2\theta \leq 80°$ with a scanning step of 0.02° and a fixed counting time of 10 s. Divergence, scattered and receiving radiation slits were 1°, 1° and 0.2 mm respectively. The $KSr_2Nb_5O_{15}$ structure was refined according to the Rietveld method using the FullProff program [33]. The parameters and variables adopted during the refinement process were the background coefficients, and isotropic atomic displacement parameters for four kinds of atoms (K, Sr, Nb, O). In addition, profile coefficients, histogram scale, lattice parameters, linear absorption coefficients, and oxygen parameters ($X$) were also estimated. The background level was fitted with a five-order polynomial function and the peak shape with a pseudo-Voigt function. The angular dependence of the peak full-width at half-maximum ($H$) was defined by a function early reported by Caglioti and co-workers [34]. Using the atomic positions derived in the refinement step, the $KSr_2Nb_5O_{15}$ unit cell was built using the Diamond software package.

Chemical bonds were analyzed by Fourier transformed infrared spectroscopy (FTIR). The sample was diluted in KBr (ratio of 1:100) and the measurements were carried out in the range of 1000–400 $cm^{-1}$ with a resolution of 1 $cm^{-1}$ for 100 scans in a Digilab Excalibur spectrometer (FTS 3100 HE series).

The microstructure and morphology was characterized using scanning electron microscopy (SEM), in a Zeiss EVO LS15 equipment at an accelerating voltage 30 kV. For SEM analysis a small amount of powder was added in ethanol and ultrasonicated for dispersion and then, a small amount of suspension was taken and dropped on the surface of a double-sided conductive carbon tape. It was then kept for some minutes at room temperature for drying. The histograms obtained from statistical processing of images were performed using the ImageJ software [35].

The density of the samples (previously outgassed at 200 °C) was determined by helium picnometry using an Accupyc 1330 (Micromeritics) apparatus thermostatically controlled with an

external circulating bath at 35 °C to avoid erroneous measurements associated to helium adsorption during density determinations [36].

The texture of the prepared materials was characterized by measuring the $N_2$ and $CO_2$ adsorption-desorption isotherms at −196 and 0 °C, respectively, in automatic volumetric analyzers (ASAP 2010, Micromeritics). The samples were previously outgassed under dynamic vacuum (ca. $10^{-5}$ Torr) at 200 °C for 17 h. Strict analysis conditions were programmed during the gas adsorption measurements to ensure equilibrium data (the average elapsed time for each isotherm was 9–12 h), with over 80 equilibrium points. Each isotherm measurement was performed in duplicate to guarantee the accuracy of the experiments (error was below 0.1%) and to obtain reproducible data. Ultrahigh purity gases (i.e., 99.9992 and 99.995% for $N_2$ and $CO_2$, respectively) were supplied by Air Products. The isotherms were used to evaluate the specific surface area (BET equation), total pore volume (evaluated at a relative pressure of 0.99) and volume of micropores evaluated from the Dubinin-Radushkevich (DR) formulism [37].

The optical features of the niobate-based materials were determined by UV–Vis diffuse reflectance spectroscopy recorded on a Shimadzu spectrometer equipped with an integrating sphere and using $BaSO_4$ as a blank reference. Measurements were recorded in the diffuse reflectance mode (R) and transformed to a magnitude proportional to the extinction coefficient through the Kubelka–Munk function, $F(R\infty)$ [38]. Band-gap energies were calculated by plotting $[F(R\infty)\cdot h\upsilon]^{1/n}$ against hυ. Each measurement was performed in triplicate to guarantee the accuracy of the experiments (error was below 2%).

### 2.3. MB adsorption in the dark and photocatalytic test

Methylene blue (MB) was analytical grade and purchased from Aldrich. An open to air batch photoreactor was employed, consisting of a 200 mL cylindrical pyrex flask provided with a bottom optical window of 6 cm in diameter, as described elsewhere [39]. Irradiation was provided using an UV–visible Hg lamp ($L_{Hg}$), and filtered by a circulating water cell (thickness ca. 2.0 cm) to remove IR beams and prevent any heating of the suspension. The UV (320–390 nm) and visible light (400–780 nm) components were estimated by integration of the radiation spectrum [27]. Total radiation was verified by using a pyranometer (Solar Light PMA2100) and the total photon flux was estimated ca. $1.23 \times 10^{17}$ photons·cm$^{-2}$·s$^{-1}$. This value corresponds to the domain. According to the literature, this value would correspond to the domain for an optimal light power utilization, where the rate of the reaction is directly proportional to the radiant flux [2].

The photocatalytic tests were performed at 25 °C under stirring 62.5 mg of the niobate-based photocatalyst in 125 mL of MB solution (initial concentration of 12.5 ppm, ca. 39.1 μmol/L). The samples were maintained in the dark at least for 60 min in order to complete adsorption at equilibrium prior the UV-irradiation of the samples. MB aliquots were taken, centrifuged and analyzed using an UV-spectrophotometer Perkin Elmer, Lambda 35 at 664 nm and the MB concentrations were estimated using a standard calibration curve. Photocatalytic tests were performed by triplicate to guarantee the accuracy of the experiments (error was below 3%). Results were compared against values obtained on a commercial $TiO_2$-P25 (Evonik, ex-Degussa) and previously reported [39].

## 3. Results and discussion

### 3.1. Characterization of solids

#### 3.1.1. X-ray diffraction (XRD)

Fig. 1A shows the XRD patterns of the $KSr_2Nb_5O_{15}$ powders obtained after calcination of the precursors for different times. As seen, the solids showed a tetragonal tungsten bronze TTB-type structure, identified according to JCPDS card number 34-0123 [11,32]. No evidences of the presence of other crystalline structures (oxides and/or carbonates) were detected in the patterns, suggesting that all the precursors were consumed during the calcination (or converted to non-crystalline phases). The present niobate-based materials showed a high crystallinity similar than those observed for $K_6Nb_{10.8}O_{30}$ [5] and for $Sr_{2-x}K_{1+x}Nb_5O_{15-x}F_x$ [40] TTB-type structures prepared by a solid-state reaction method.

By using the Jade 8 Plus software the crystallite size was derived from Scherrer's equation, Eq. (1), where $\beta$ is the broadening of the diffraction line measured at half of the maximum intensity, λ is the wavelength (Cu Kα = 1.5418 Å), θ is the Bragg angle for a given diffraction, and k is a constant, which is in general equal to 0.9 for powders.

$$D = \frac{k \cdot \lambda}{\beta \cdot \cos\theta} \quad (1)$$

The instrumental broadening effect was eliminated by subtracting the full width at half-maximum ($\beta_o$) of a standard sample ($SiO_2$) from $\beta$ of the respective Bragg peaks. The lattice strain was estimated using the Williamson-Hall approach [41] according to Eq. (2), where D represents the crystallite size estimated from Eq. (1) and η represents the lattice strain.

$$\beta\frac{\cos(\theta)}{\lambda} = \frac{1}{D} + 4\eta\frac{\sin(\theta)}{\lambda} \quad (2)$$

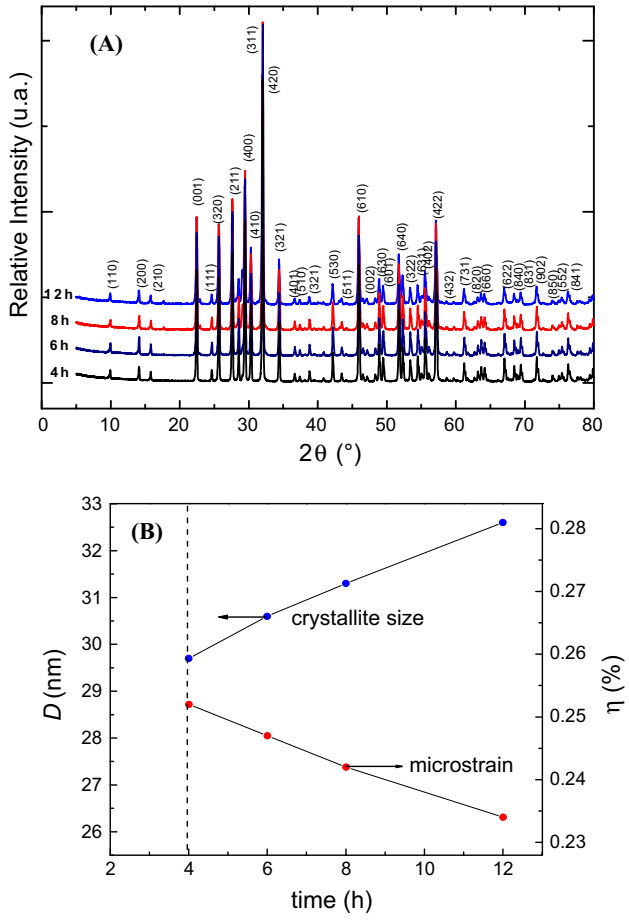


**Fig. 1.** (A) XRD patterns for the $KSr_2Nb_5O_{15}$ $KSr_2Nb_5O_{15}$ nanostructured powders. (B) Average crystallite size and lattice strain evolution as a function of thermal treatment time at 1100 °C.

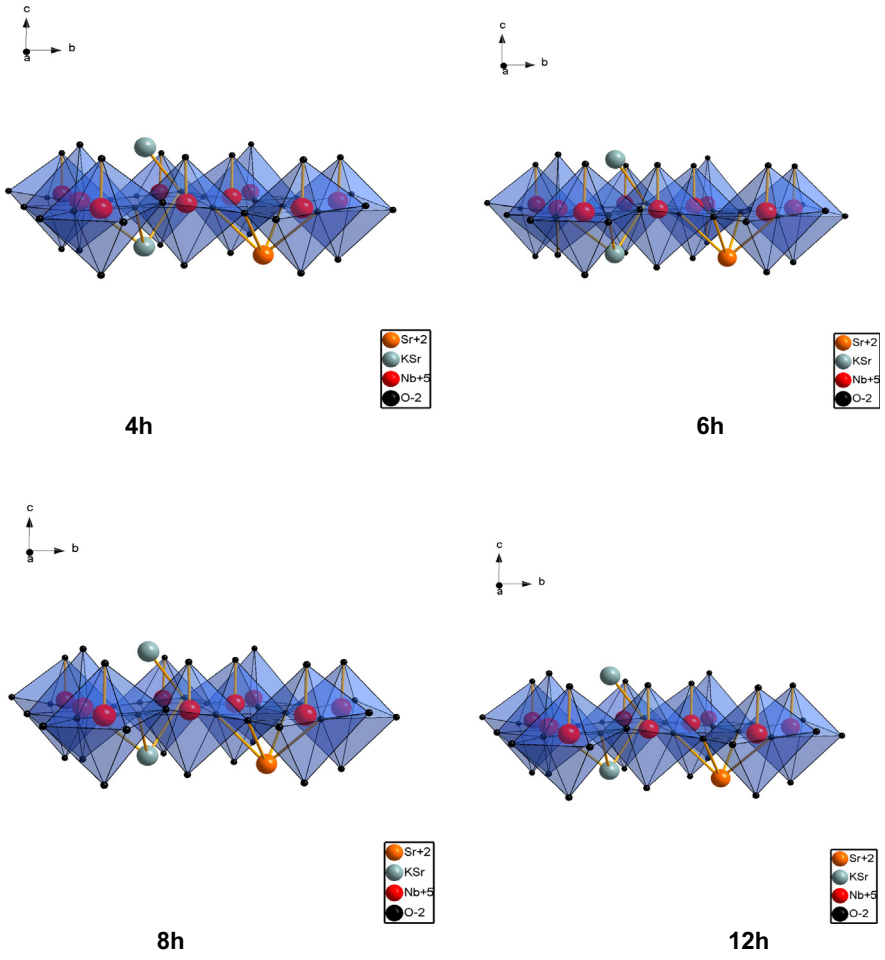


**Fig. 2.** Graph of the unit cell for $KSr_2Nb_5O_{15}$ precursor powder calcined at 1100 °C for, 4, 6, 8 and 12 h. View in the c axis direction

The characteristic Williamson-Hall plot corresponds to the graph of [βcos(θ)/λ] as a function of [4sin(θ)/λ]. Here, [4sin(θ)/λ] is on the x-axis. Each point is assigned to a specific diffraction line and after point collection, a linear regression fit was obtained. The crystallite size (D) corresponds to the y-intercept and the lattice strain (η) was obtained from the slope of the fit curve.

Fig. 1B shows the average crystallite size and the lattice strain of the $KSr_2Nb_5O_{15}$ nanostructured powder as a function of the calcination time. As seen, rising the calcination time resulted in an increase in the crystallite size and a decrease in the microstrain lattice, with the highest average crystallite size of 32.5 nm obtained after 12 h of calcination. The increase in the average crystallite size as a function of the calcination time has been attributed to the particle growing and agglomerate development by the densifying mechanism [42,43], which is strongly dependent on the temperature and time of the thermal treatment.

### 3.1.2. Structural refinements

The X-ray diffraction patterns of the $KSr_2Nb_5O_{15}$ materials were indexed on the basis of a tetragonal unit cell. The structural parameter set of the samples was derived using the Rietveld method. The refinements of the structural parameters were performed by taking into account the space groups *P4bm* (No. 100), that are compatible with the rule of existence [(*0 k l*) *k* = 2*n*] [11,32,40]. Data and experimental conditions for the structural refinements are listed in Table S1 in the Supplementary Material. Further theoretical adjustment for the $KSr_2Nb_5O_{15}$ phase was obtained assuming that each pentagonal site [4c(x, x + 1/2, z)] was statistically occupied by equal quantities of $K^+$ and $Sr^{2+}$ ions and each tetragonal site [2a(0, 0, z)] was occupied by a $Sr^{2+}$ ion. The trigonal site was considered vacant. Refinement data of showed major isotropic atomic displacement parameter $B_{eq}$ values for the sample calcined for 4 h. Because the $B_{eq}$ parameter is related to the degree between disorder/order, a higher $B_{eq}$ value suggests a significant degree of disorder in the structure [40]. It is possible to hypothesize that the $KSr_2Nb_5O_{15}$ materials exhibited a residual static disorder that is correlated to the A and B site occupation and $Nb^{5+}$ cation off-center. This feature is compatible with a process of rearrangement and the growth of crystallites from the sintering of nanostructures [11], as discussed above.

Fig. S1 shows the graphic representation of the unit cell of the $KSr_2Nb_5O_{15}$ powders calcined for different times, in the view of the b axis direction. The front view (b axis direction) shows that the Nb atoms are tilted and coordinated to six oxygen atoms, four of which are located, *a priori*, on the same plane as the niobium atoms. The other two are above and below the plane, respectively. More valuable information can be obtained from Fig. 2, showing a graphic representation of the unit cell of the series of $KSr_2Nb_5O_{15}$ powders in the view of the c axis direction. In this case, the position of Nb atoms tends to be located at the center of the polyhedron with the decreasing of the Nb—O bonds lengths related to the niobium with the apical oxygens. The Nb—O bond lengths are shown in Table 1. In the $KSr_2Nb_5O_{15}$ structure, the $Nb^{5+}$ cations can be differentiated as Nb(1) and Nb(2) because they occupy two non-equivalent octahedral sites called B1 (*2b* sites) and B2 (*8d* sites) [11,32]. Table 1 shows the interatomic distances of the Nb—O

**Table 1**
Interatomic distances of Nb—O bonds on the octahedral sites of $KSr_2Nb_5O_{15}$ with the calcination time.

| | | | | | | |
|---|---|---|---|---|---|---|
| KSrNb-4 h | | | | | | |
| $[Nb^{5+}(1)O_6]$ Octahedron ($KSr_2Nb_5O_{15}$) - Atom: Nb(1) Wyckoff position: *2b** | | | | | | |
| Bonds | Nb—O(1) | Nb$^{\xi}$—O(2) | Nb$^{\xi}$—O(3) | Nb$^{\xi}$—O(4) | Nb$^{\xi}$—O(5) | Nb—O(6) |
| d (Å) | 2.1570 (12) | 1.8565 (14) | 1.8565 (14) | 1.8565 (14) | 1.8565 (14) | 1.8107(12) |
| $[Nb^{5+}(2)O_6]$ Octahedron ($KSr_2Nb_5O_{15}$) - Atom: Nb(2) - Wyckoff position: *8d** | | | | | | |
| Bonds | Nb—O(1) | Nb$^{\xi}$—O(2) | Nb$^{\xi}$—O(3) | Nb$^{\xi}$—O(4) | Nb$^{\xi}$—O(5) | Nb—O(6) |
| d (Å) | 1.7908 (6) | 1.9664 (2) | 1.9991 (2) | 2.0219 (17) | 2.0580 (17) | 2.1515 (6) |
| KSrNb-6 h | | | | | | |
| $[Nb^{5+}(1)O_6]$ Octahedron ($KSr_2Nb_5O_{15}$) - Atom: Nb(1) Wyckoff position: *2b** | | | | | | |
| Bonds | Nb—O(1) | Nb$^{\xi}$—O(2) | Nb$^{\xi}$—O(3) | Nb$^{\xi}$—O(4) | Nb$^{\xi}$—O(5) | Nb—O(6) |
| d (Å) | 2.1105 (10) | 1.8675 (9) | 1.8675 (9) | 1.8675 (9) | 1.8675 (9) | 1.8315(10) |
| $[Nb^{5+}(2)O_6]$ Octahedron ($KSr_2Nb_5O_{15}$) - Atom: Nb(2) - Wyckoff position: *8d** | | | | | | |
| Bonds | Nb—O(1) | Nb$^{\xi}$—O(2) | Nb$^{\xi}$—O(3) | Nb$^{\xi}$—O(4) | Nb$^{\xi}$—O(5) | Nb—O(6) |
| d (Å) | 1.8003(2) | 1.9660(5) | 2.0009(5) | 2.0218(5) | 2.0586(5) | 2.1545(4) |
| KSrNb-8 h | | | | | | |
| $[Nb^{5+}(1)O_6]$ Octahedron ($KSr_2Nb_5O_{15}$) - Atom: Nb(1) Wyckoff position: *2b** | | | | | | |
| Bonds | Nb—O(1) | Nb$^{\xi}$—O(2) | Nb$^{\xi}$—O(3) | Nb$^{\xi}$—O(4) | Nb$^{\xi}$—O(5) | Nb—O(6) |
| d (Å) | 2.0868 (12) | 1.8791 (12) | 1.8791 (12) | 1.8791 (12) | 1.8791 (12) | 1.8506(12) |
| $[Nb^{5+}(2)O_6]$ Octahedron ($KSr_2Nb_5O_{15}$) - Atom: Nb(2) - Wyckoff position: *8d** | | | | | | |
| Bonds | Nb—O(1) | Nb$^{\xi}$—O(2) | Nb$^{\xi}$—O(3) | Nb$^{\xi}$—O(4) | Nb$^{\xi}$—O(5) | Nb—O(6) |
| d (Å) | 1.8001 (5) | 1.9500 (2) | 2.0178 (2) | 2.0349 (2) | 2.1022 (16) | 2.1273 (5) |
| KSrNb-12 h | | | | | | |
| $[Nb^{5+}(1)O_6]$ Octahedron ($KSr_2Nb_5O_{15}$) - Atom: Nb(1) Wyckoff position: *2b** | | | | | | |
| Bonds | Nb—O(1) | Nb$^{\xi}$—O(2) | Nb$^{\xi}$—O(3) | Nb$^{\xi}$—O(4) | Nb$^{\xi}$—O(5) | Nb—O(6) |
| d (Å) | 2.1816 (7) | 1.8853 (13) | 1.8853 (13) | 1.8853 (13) | 1.8853 (13) | 1.7650(7) |
| $[Nb^{5+}(2)O_6]$ Octahedron ($KSr_2Nb_5O_{15}$) - Atom: Nb(2) - Wyckoff position: *8d** | | | | | | |
| Bonds | Nb—O(1) | Nb$^{\xi}$—O(2) | Nb$^{\xi}$—O(3) | Nb$^{\xi}$—O(4) | Nb$^{\xi}$—O(5) | Nb—O(6) |
| d (Å) | 1.8386 (5) | 1.9753 (2) | 2.0059 (19) | 2.0115 (15) | 2.0604 (7) | 2.1375 (5) |

d is the interatomic distance (Å). ξ indicates the oxygen atoms of the central plane of octahedra.

bonds in both $[Nb(1)O_6]$ and $[Nb(2)O_6]$ octahedral sites of $KSr_2Nb_5O_{15}$ precursor powder calcined for 4, 6, 8 and 12 h at 1100 °C. For the $[Nb(1)O_6]$ octahedron, all four bond lengths of the central plane (indicated by ξ) are similar. Counter clockwise, four distinct bond lengths are derived in the $[Nb(2)O_6]$ octahedron indicating some degree of rotation and tilting. The Nb—O bond lengths of the Nb (2) that constitutes the central plane of the octahedron, denoted as Nb—O(2), Nb—O(3), Nb—O(4), and Nb—O(5) are different, and such distortion seems be compatible with some rotation degree along of the c-axis. This rotation can be clearly observed for the sample calcined for 6 h. Furthermore, the set of four distinct bond lengths indicates a slight degree of tilting of the octahedron. Therefore, distortions of the $[Nb(2)O_6]$ octahedron involve six vertices. This tilting can be clearly observed for the sample calcined for 6 h. This property is responsible for the increase in the Nb—O(6) bond length in the $[Nb(2)O_6]$ octahedron related to the apical oxygen (6), as shown in Table 1. The highest increase in the Nb—O(6) bond length was found for the $KSr_2Nb_5O_{15}$ precursor powder calcined for 6 h. The role of the increase in the Nb—O(6) bond lengths, which is intimately related with the reactivity of the apical oxygen atoms in the niobate structure, on the photocatalytic activity of these materials will be discussed below.

### 3.1.3. Scanning electron microscopy (SEM)

SEM has been used to explore the morphology of the photocatalyst's nanoparticles and the degree of aggregation in solid state. The size and morphology of the photocatalysts calcined at 1100 °C for 4 h and 12 h was investigated by scanning electron microscopy (SEM). The micrograph in Fig. 3A corresponding to sample KSrNb-4 shows quasi-spherical particles with several sizes, indicating the occurrence of some degree of particle's coalescence and aggregation between the particles. Different to this quasi-spherical morphology, previous works for $KNb_3O_8$ [4] and $K_6Nb_{10.8}O_{30}$ [5] prepared by a solid-state reaction method showed a nearly tetragonal columnar-shaped crystalline particles [4,5].

The size of the present primary particles should be in the order of 35 nm because the coalescence actuates mainly on the secondary particles, giving rise to particles of sizes ranging from 50 to 90 nm. At converse, in the case of the sample calcined for 12 h (KSrNb-12), there does not seem to be a preferential particle growth by coalescence. The micrograph in Fig. 3B shows a narrow range of nanoparticle sizes between 50 and 200 nm (i.e. 94 and 85 % nanoparticles in this range for KSrNb-4 and KSrNb-12, respectively); the nanoparticles of sample KSrNb-12 also exhibit different levels of distortion, suggesting that the coalescence is not spontaneous. Moreover, in this stage, the particles are already ferroelectric, what in fact prevents the growth activation by coalescence [42,43].

The present niobate-based materials showed a much lower average size than those observed by Zhang and co-workers [4,5] with average sizes around 1.5 μm [4], and in the range of 0.5–1.2 μm for $KNb_3O_8$ [4] and $K_6Nb_{10.8}O_{30}$ [5] TTB-type structures prepared by a solid-state reaction method.

### 3.1.4. Density and texture of samples

The present work include by the first time a complete textural characterization by $N_2$ and $CO_2$ adsorption-desorption isotherms, Hg porosimetry and He picnometry. The porosity of the

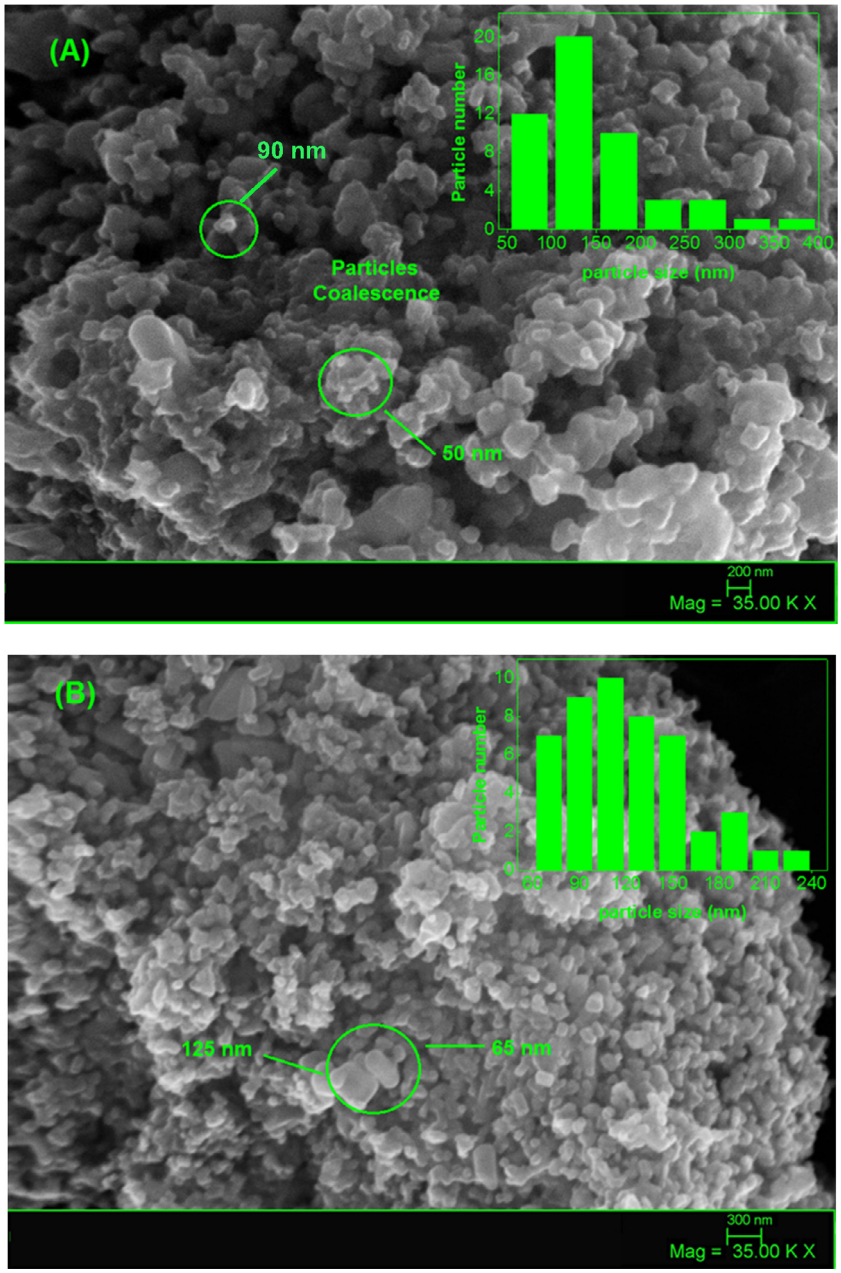


**Fig. 3.** Scanning electron microscopy (SEM) images of $KSr_2Nb_5O_{15}$ powders. (A) Calcined at 1100 °C for 4 h. (B) Calcined at 1100 °C for 12 h.

synthesized niobate-based materials was evaluated by gas adsorption and helium picnometry. The main textural parameters are compiled in Table 2 (the corresponding experimental adsorption-desorption $N_2$ isotherms at −196 °C are shown in Fig. S2). Data corresponding to $TiO_2$ benchmark is also included for comparison purposes. All the samples presented reversible type II isotherms according to the IUPAC classification [44], characterized by a smooth curvature at low relatives pressures and a lack of hysteresis loop in the desorption branch, typical of non-porous solids. The textural parameters calculated from the $N_2$ adsorption isotherms confirmed the low porous features of all the samples in terms of low surface area values and micropore volumes (Table 2). The specific BET surface area values ranged from 2 to 3 $m^2\ g^{-1}$, and the microporosity was negligible (about 0.001 $cm^3\ g^{-1}$) for the four samples. The narrow microporosity was also evaluated by means of the $CO_2$ adsorption-desorption isotherms at 0 °C (also shown in Fig. S2), and data compiled in Table 2 reveled a similar trend. Hence, the porosity of the samples is mainly associated to external area. Overall, no significant differences were obtained among the samples obtained at different calcination times, despite the variation in the average particle size observed in the SEM images (Fig. 3).

Helium density values of ca. 5 g $cm^{-3}$ were obtained for all the samples, regardless the calcination temperature (Table 2) suggesting a high sintering effect in the materials even after calcination for short periods. A similar effect has been described elsewhere by Pullar and co-workers [45] for other types of niobate-based materials. The density values calculated by helium pycnometry can be ascribed to the so-called particle density for non-porous solids.

### 3.1.5. Infrared spectroscopy with Fourier transformed (FTIR)

Fig. 4 shows the FTIR transmittance spectrum in the region between 400–1000 $cm^{-1}$ of the $KSr_2Nb_5O_{15}$ powders obtained after thermal treatment of the precursor powder at 1100 °C for 4, 6, 8 and 12 h. All spectra showed six absorption bands of

**Table 2**
Main nanotextural properties of the synthesized materials obtained from gas adsorption data and helium picnometry.

| Samples | He density[a] | $N_2$ @ −196 °C | | | | $CO_2$ @ 0 °C |
|---|---|---|---|---|---|---|
| | | $S_{BET}$[b] | $V_{total}$[c] | $S_{external}$[d] | $W_{o,N2}$[e] | $W_{o,CO2}$[e] |
| | g /cm$^3$ | m$^2$/g | cm$^3$/g | m$^2$/g | cm$^3$/g | cm$^3$/g |
| KSrNb-4 h | 5.00 | 2.7 | 0.005 | 2.4 | 0.001 | 0.001 |
| KSrNb-6 h | 5.00 | 2.8 | 0.005 | 2.7 | 0.001 | 0.001 |
| KSrNb-8 h | 5.00 | 2.4 | 0.004 | 2.4 | 0.001 | 0.001 |
| KSrNb-12 h | 5.00 | 3.1 | 0.006 | 2.9 | 0.001 | 0.002 |
| $TiO_2$-P25 | 3.84 | 53 | 0.118 | 51.3 | 0.019 | 0.006 |

[a] Density measured in a He pycnometer.
[b] Specific surface area determined by the BET equation.
[c] Total pore volume evaluated at relative pressure 0.99.
[d] External surface area evaluated using the *t*-plot method.
[e] Micropore volume evaluated from the Dubinin–Radushkevich equation applied to either the $N_2$ or $CO_2$ adsorption isotherm.

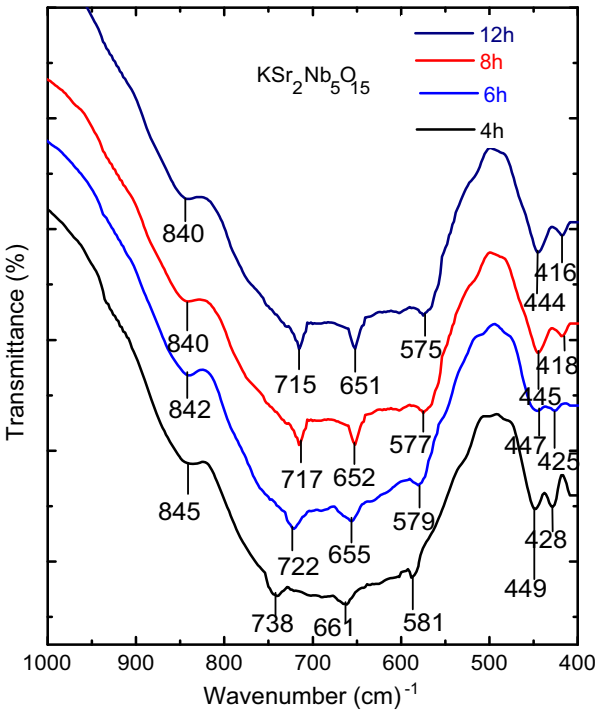


**Fig. 4.** FTIR transmittance spectrum of the $KSr_2Nb_5O_{15}$ powders obtained after thermal treatment at 1100 °C for 4, 6, 8 and 12 h.

middle-high intensity centered between 845 and 416 cm$^{-1}$. Only absorption bands at high wavenumbers are clearly observed while the rest show overlapping of bands. All bands were assigned to Nb—O bonds [32,46]. The vibrational band observed at around 416 cm$^{-1}$ has been attributed to the normal mode of vibration, associated to binding of niobium to oxygen apical octahedron [$NbO_6$], previously reported [8,32,46]. According to Fig. 4, the FTIR spectra show a shift of the bands to lower wavenumbers when the calcination time is increased. This shift to lower wavelengths is an evidence of a decrease in Nb—O bonds length. The FTIR results are in according with structural parameters data discussed above, and can be associated to the decreasing in the covalent character of the bond Nb—O, associated with an increased ionic character [8]. Above 8 h of calcination, the shift in the spectra is no longer evidenced - samples calcined for 8 and 12 h showed practically similar spectra-, indicating that the maximum sintering effect is achieved after 8 h calcination [45].

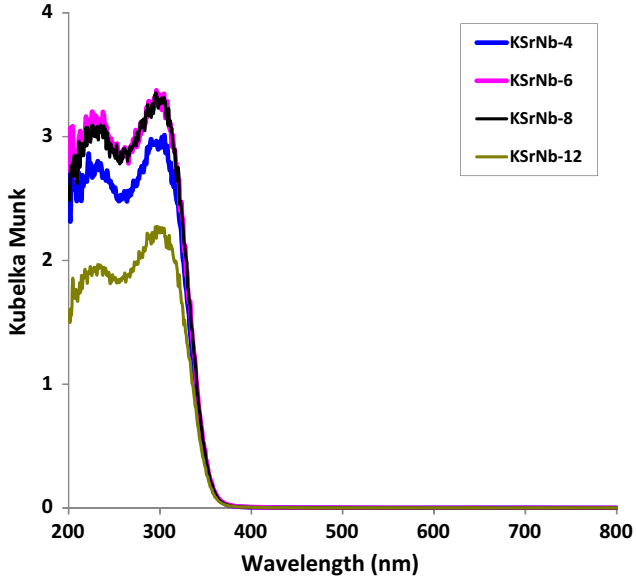


**Fig. 5.** UV–vis/DR spectra of the niobate-based materials.

### 3.1.6. UV–Vis/DR spectroscopy

The optical properties of $KSr_2Nb_5O_{15}$ samples were studied by diffuse reflectance (DRS) spectroscopy in the UV–visible range (ca. 200–800 nm). The corresponding spectra are shown in Fig. 5 and displayed the typical absorption band edge below 360 nm, ascribed to the transitions of electrons from 2p orbitals in O atoms to 3d orbitals in Nb atoms, contributing to the formation of the valence and conduction bands responsible for the band-gap [47]. There is almost no difference in the location of the absorption band edge of the different samples, indicating that the calcination does not modify the optical band gap. The band gap energies of the samples can be estimated from the tangent lines in the plots of the modified Kubelka-Munk function versus the energy of exciting light [38,48] by considering $KSr_2Nb_5O_{15}$ as an indirect semiconductor [38,47,48]. The obtained values were similar for all the samples (ca. 3.5 eV), and very similar to those reported by Zhang and coworkers for non-complex structural niobate-based materials such as $KNbO_3$ crystals [6] (ca. 3.47 eV). By contrast, same authors reported [49] a lower value (ca. 3.3 eV) for $KSr_2Nb_5O_{15}$ showing a micrometric structure and prepared by a solid-state method that involves conventional mechanical mixture of solids followed by calcination. These differences have to be attributed to the mixing procedure of the precursors, since the methodology reported in this work involves a (strong) high-energy ball milling procedure

followed by a controlled calcination, as opposed to the (soft) conventional mechanical mixture reported Zhang et al. So, the UV–vis spectra showed in Fig. 5 demonstrates that herein synthesized $KSr_2Nb_5O_{15}$ materials can be catalogued as indirect semiconductors photoactive in the UVA range [6,49].

### 3.2. MB adsorption and photocatalytic test

Fig. 6 shows the kinetics of methylene blue (MB) adsorption in the dark along with the kinetics of MB photodegradation under UV–visible irradiation. The corresponding kinetic parameters therein evaluated are compiled in Table 3. The performance of herein synthesized $KSr_2Nb_5O_{15}$ nanostructured materials has been compared to that of commercial titania powders, for clarity. It can be seen that the adsorption rate is very fast for all the catalysts, reaching the equilibrium uptake for the adsorption of the dye after 30–60 min (Fig. 6A). Accordingly, the photocatalytic tests under UV–vis irradiation were conducted after an initial period of 60 min adsorption. It is interesting to remark that the amount of MB adsorbed decreased with the calcination time (ca. 0.863 vs 1.123 μmol, for calcination during 12 and 4 h, respectively). This effect cannot be attributed to a decrease in the surface area of the samples, since all of them displayed similar porous features as discussed above (Table 2); on the other hand, it has been reported that long periods of calcination promote the sintering of niobate-based samples [45], therefore leading to higher mean crystal size of the particles. This sintering effect was also confirmed by the SEM images (Fig. 3) and the XRD refinements, with the highest average crystallite size obtained after 12 h calcination.

It is important to point out that KSrNb-4 sample adsorbed almost the same amount of MB than $TiO_2$ powders, despite the surface area of the latter is remarkably higher (Table 2). However, this was rather expected due to the chemical nature of methylene blue; being a strong Lewis base, its adsorption is thermodynamically favored on acid Lewis solids such as herein synthesized niobate-based materials. Indeed, a stronger acid Lewis character is expected for the prepared niobate-based nanostructured materials than for $TiO_2$ because of the high electron affinity of Nb ions (i.e. 86.1 kJ/mol compared to 7.6 kJ/mol for Ti ions).

For a better understanding of the influence of the methylene blue adsorption on the photocatalytic activity of the studied materials, the surface concentration ($d_{MB}$) of the adsorbed MB molecules on the $KSr_2Nb_5O_{15}$ materials was estimated as [50,51]:

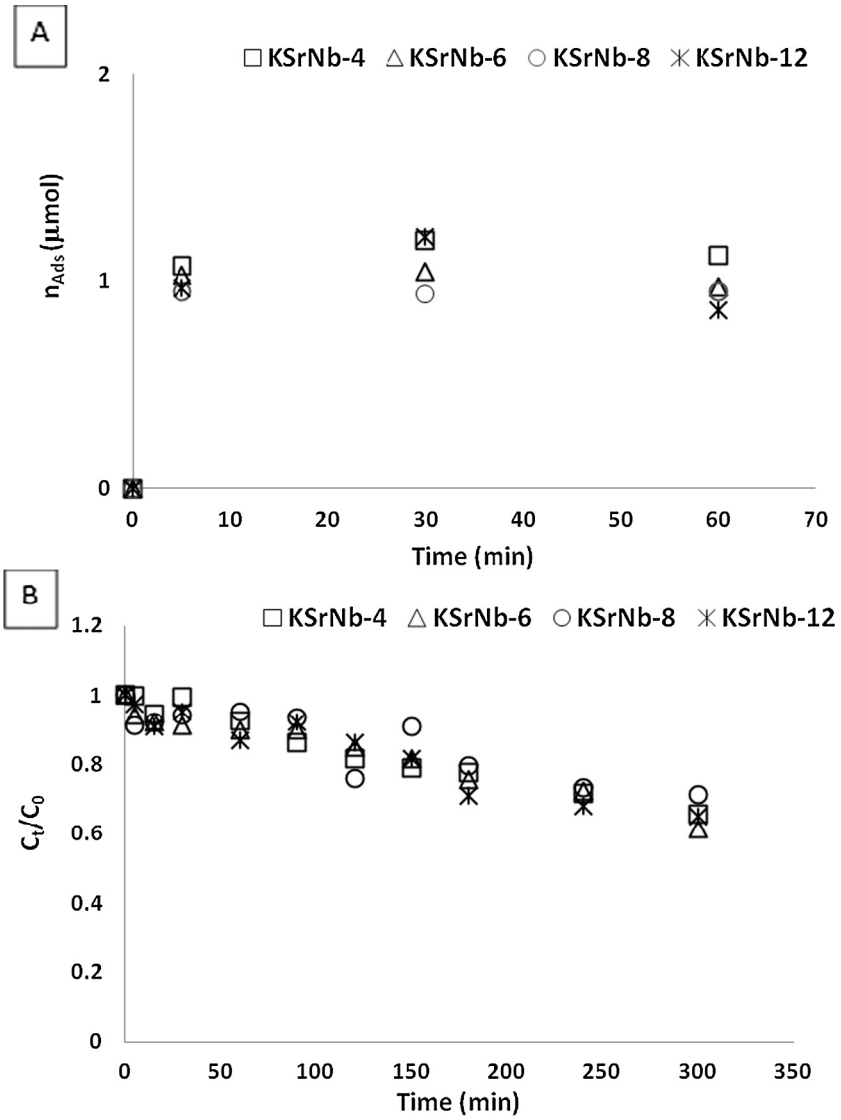


**Fig. 6.** Kinetics of MB adsorption in the dark (A), and MB photodegradation (B) on $KSr_2Nb_5O_{15}$ samples.

**Table 3**
MB adsorption in the dark ($n_{ads}$), first-order apparent rate-constant ($k_{app}$), and reaction-rate ($v_{reac}$) for MB photodegradation on $KSr_2Nb_5O_{15}$.

| Sample | $n_{ads}$ (μmol)[b] | $d_{MB}$ (μmol·m$^{-2}$)[c] | $k_{app}$ (min$^1$)[d] ×10$^{-3}$ | $R^2$[e] | $v_{reac}$ ×10$^{-3}$ (μmol·m$^{-2}$·min$^{-1}$)[f] | $\Phi_{rel}$[g] |
|---|---|---|---|---|---|---|
| $TiO_2$-P25 | 1.222[a] | 0.391 | 6.05[a] | 0.9952 [a] | 2.37 | 1.00 |
| KSrNb-4 | 1.123 | 6.655 | 1.42 | 0.9781 | 9.45 | 3.99 |
| KSrNb-6 | 0.972 | 5.554 | 1.64 | 0.9842 | 9.11 | 3.84 |
| KSrNb-8 | 0.950 | 6.333 | 1.22 | 0.9494 | 7.73 | 3.26 |
| KSrNb-12 | 0.863 | 4.454 | 1.30 | 0.9245 | 5.79 | 2.44 |

[a] Values taken from Ref. [36].
[b] MB absorbed in the dark after 60 min (Fig. 6A).
[c] Surface concentration MB molecules estimated by Eq. (3).
[d] $k_{app}$ estimated by Eq. (4).
[e] $R^2$ is the factor linear regression.
[f] Reaction-rate estimated by Eq. (6).
[g] Photoactivity relative to $TiO_2$. $\Phi_{rel} = v_{reac\text{-}i}/v_{reac\text{-}TiO2}$.

$$d_{MB} = n_{ads}/S_{BET} \cdot m \quad (3)$$

where $n_{ads}$ is the amount of adsorbed MB in the dark after 60 min (Table 3), $S_{BET}$ is the surface area estimated by BET equation (Table 2), and m is the mass of solid (i.e., 62.5 mg). Data corresponding to $TiO_2$ is also included in Table 3 for comparison purposes [39].

Despite the surface area of $TiO_2$ is more than one order magnitude higher than the values of the $KSr_2Nb_5O_{15}$ materials, the latter showed a much higher MB surface concentration than $TiO_2$. This is in agreement with the fact that the niobate-based catalysts present a more acid surface pH than $TiO_2$ [21], and accordingly, have a high affinity towards basic amines such as MB with a high dissociation constant ($pK_b$) in water and a high half neutralization potential [52]. No clear correlation was observed between the calcination time and/or the surface area of the niobates and the MB surface concentration, despite the lowest value was found for the sample calcined for the longest time.

On the other hand, Fig. 6B shows very similar kinetics trends in the photocatalytic degradation of MB for all the $KSr_2Nb_5O_{15}$ photocatalysts. In order to compare the photoactivity, the first-order apparent rate-constants ($k_{app}$) were estimated from the linear regression of the kinetic data in Fig. 6B, using equation 4 and assuming that MB photodegradation follows a first-order reaction-rate mechanism [50,51]:

$$Ln(C_o/C_t) = k_{app} \cdot t \quad (4)$$

where $C_o$ is the MB concentration after achieved the adsorption equilibrium in the dark and $C_t$ the MB concentration at time t. The $k_{app}$ values are included in Table 3 as well as the factor linear regression ($R^2$) which values were in all cases close to 1 indicating that the assumption of a first-order reaction-rate mechanism was correct.

It can be inferred from Table 3 that the dependence of the photoactivity ($k_{app}$) and the calcination time of the prepared materials followed a Vulcan-type trend. The $k_{app}$ reached a maximum of $1.64 \times 10^{-3}$ min$^{-1}$ for the KSrNb-6 h, and then the photoactivity monotonically decreased when the catalysts were calcined for longer periods of time. We have attributed this maximum in the photoactivity to the presence of tilted and very reactive apical oxygen atoms bonded to niobium in the [$NbO_6$] octahedron as suggested by the XRD refinement analysis discussed above (Table 1, Fig. 2). In addition, the increase in the average crystallite size as a function of the calcination time was well correlated with the photoactivity, indicating that an optimal aggregate development of the niobate-based materials is required to achieve a good photocatalytic performance. A similar behavior was reported for hybrid $TiO_2$-C binary materials during the photocatalytic degradation of 4-chlorophenol [53].

### 3.3. General discussion

In terms of the first-order apparent rate-constants (Table 3), it must be pointed out that all niobates-based materials showed lower photoactivity than commercial $TiO_2$. Based on the non-porous nature of the solids (Table 2), the conversion of methylene blue is most likely attributed to a series of chemical reactions occurring in the external surface of the materials. Thus, a deepest analysis of the photocatalytic activity can be performed to obtain the global reaction rate ($v_{reac}$) considering the MB surface concentration ($d_{MB}$) estimated above (Table 3), since this primary fraction of MB molecules will suffer the photodegradation.

The photocatalytic degradation of MB can be considered as an unimolecular catalytic surface reaction [2,12,50,51], where the MB adsorption followed by photodegradation under UV–vis irradiation can be described by Eq. (5).

$$MB + S \rightleftharpoons MB_{Ads} \rightarrow \text{Intermediates} \rightarrow \text{Products} \quad (5)$$

where MB is the reactant, S an adsorption site on the surface niobate-based and $TiO_2$ photocatalysts, and $MB_{Ads}$, the MB adsorbed after achieved the steady-state condition of adsorption in the dark.

The reaction rate ($v_{reac}$) can be estimated [2,22] by Eq. (6), where $v_{reac}$ is expressed in μmol m$^{-2}$ min$^{-1}$ and $d_{MB}$ is the surface concentration of MB on $KSr_2Nb_5O_{15}$ or $TiO_2$.

$$V_{reac} = k_{app} \cdot d_{MB} \quad (6)$$

The values for $v_{reac}$ are included in Table 3. It can be seen that the $v_{reac}$ obtained on $TiO_2$ was clearly lower than the values of any of the studied $KSr_2Nb_5O_{15}$ materials. It is also important to note that there is a monotonic decrease in the $v_{reac}$ with increasing the calcination time. In other words, the reaction rate for the degradation methylene blue was faster for the photocatalysts calcined during lower times. The higher the photocatalytic activity relative to $TiO_2$ ($\Phi_{rel}$) was achieved for the sample calcined 4 h, with a value up to about 4 times higher than that of titania. These results suggest that changes in the crystalline structure of the niobate-based materials (mainly, the increase in the Nb—O(6) bond lengths discussed above) would remarkably influence the photocatalytic activity. Indeed, the FTIR results (Fig. 4) showed a direct correlation between the wavenumber of bands and the magnitude of displacement of the Nb location off-center as a function of the increasing the calcination time of the $KSr_2Nb_5O_{15}$ powders. In addition, the structural refinement showed that the magnitude of the displacement of the Nb from the central position of the [$NbO_6$] octahedron can be ascribed to the displacement parameter ΔZ. Taking into account the [$NbO_6$] octahedron for the second Nb atom indicated as [$Nb^{5+}(2)O_6$] in Table 1, the difference between both niobium-oxygen bond lengths for the two apical oxygen atoms estimated by the Eq. (7), is proportional to twice the niobium off-center displacement Δz along the polar direction.

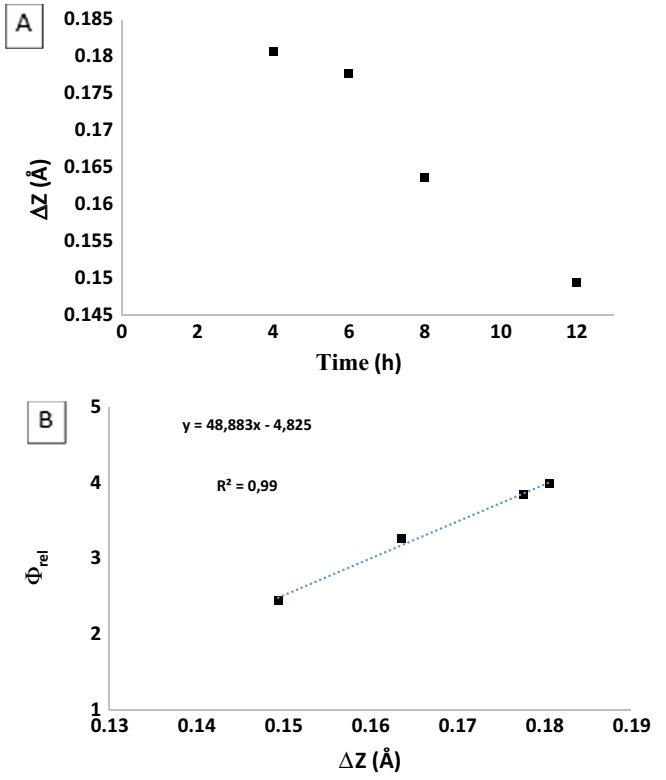


**Fig. 7.** (A) Displacement parameter ΔZ, estimated from {[Nb—O(6)] – [Nb—O(1)]} as a function of calcination time of $KSr_2Nb_5O_{15}$ precursor powder at 1100 °C. (B) Relationship between relative photoactivity and ΔZ.

$$\Delta Z = [Nb—O(6)] - [Nb—O(1)] \quad (7)$$

In consequence, the ΔZ parameter is proportional to the polarization of the structure and therefore influence the chemical reactivity as well as the optoelectronic properties [54]. Fig. 7A shows the ΔZ values (corrected after divide the difference by 2) as a function of the calcination time of $KSr_2Nb_5O_{15}$. Structural changes are expected to affect the magnitude of the spontaneous polarization ($P_S$) of $KSr_2Nb_5O_{15}$, which depends on the displacement ΔZ of $Nb^{5+}$ from the center of the [$NbO_6$] octahedron [32] as discussed in Fig. 2. According to Fig. 7A the decrease of the niobium oxygen apical bond lengths {[Nb—O(6)] – [Nb—O(1)]} as a function of the calcination time can be related with a decrease in the charge density on the surface of the material, resulting in a lower surface chemistry activity. It can be seen from the ΔZ parameter in Fig. 7A and $k_{app}$ and $v_{reac}$ values in Table 3, that the higher the displacement Δz parameter the higher the photoactivity in $KSr_2Nb_5O_{15}$.

In other words, the higher the {[Nb—O(6)] – [Nb—O(1)]} the higher the polarization of the structure and accordingly, a higher surface chemistry reactivity is expected even when the surface area of $KSr_2Nb_5O_{15}$ is very low. The influence of the displacement parameter (ΔZ) and the photocatalytic activity can be clearly seen in Fig. 7B where a linear correlation was found with a linear factor regression of 0.9936 very close to 1.

In addition, it is well-know that apical oxygen atoms play an important role in the hole density distribution and spin–spin correlation functions in high-temperature superconductors [55]. This apical oxygen is very reactive and under UV–vis irradiation it would lead to the formation of superoxo radical anion ($O_2^-$), responsible of the photodegradation of organic molecules such as MB [2,3] by electrophilic unimolecular reactions [56]. However, it is quite unclear how the apical oxygen can directly participate in formation of superoxide radical. For example, it could be eliminated and couples to other apical oxygen to form $O_2^-$. Most probably, it is the most active O in the sense of probability of the charge transfer to outer $O_2$ molecules and therefore, the higher content of such distorted Nb—O bond the higher is the efficiency of the electron transfer and the higher is the photocatalytic activity. Otherwise, it can serve as a more active center for the hole trapping which is not discussed in the present work. So, well-known trapping experiments [57,58] on the nature of dominant reactive oxygen species are ongoing in our group to elucidate this matter.

In short, the above structural evidences and the photocatalytic results suggest that the increase in the photocatalytic activity of $KSr_2Nb_5O_{15}$ can be due to the formation of highly reactive species formed in the apical oxygen atoms. To our knowledge, the correlation between ΔZ and the photocatalytic activity is herein reported for the first time. The dependence of the photocatalytic activity with the length of the Nb—O bonds to apical oxygen atoms is quite unusual, and it sheds more light on the mechanistic nuances of the photocatalytic behavior of Nb-based photocatalysts.

## 4. Conclusions

We have prepared a series of $KSr_2Nb_5O_{15}$ photocatalysts from a facile synthetic route based on a high-energy ball milling followed by calcination of oxides and carbonates of the metallic precursors. The unit cell of the synthesized $KSr_2Nb_5O_{15}$ powders showed that each pentagonal site is statistically occupied by equal quantities of $K^+$ and $Sr^{2+}$ ions, and each tetragonal site is occupied by a $Sr^{2+}$ ion. A high distortion of the [$Nb(2)O_6$] octahedra occurs due to contributions from both rotation and tilting and the spontaneous polarization is a function of the magnitude of the parameter displacement of the Nb atom from the octahedron center. The decrease of the thermal treatment time leads to an increase in the spontaneous polarization due an increase of the Nb—O bonds lengths related to the niobium with the apical oxygen in the [$NbO_6$] octahedron. These changes increased the charge density on the surface of the material, resulting in a higher superficial chemistry activity. The characterization of the optical features by UV–Vis diffuse reflectance and the kinetics of MB photodegradation confirmed the photocatalytic activity of all the $KSr_2Nb_5O_{15}$ materials and regardless the calcination temperature. It was found that the lower the calcination time, the higher the photocatalytic activity, with sample KSrNb-4 h exhibiting almost 4 times higher photocatalytic activity than commercial $TiO_2$. From the photocatalytic activity estimated in terms of reaction rates, it can be concluded that herein synthesized $KSr_2Nb_5O_{15}$ materials can be used for photocatalytic processes under very low concentration conditions under UV irradiation.

## Acknowledgments

J. Matos thanks to the Chilean grants (Basal Program PFB-27, FAE-829, FONDEF-IDEA #ID15I10321, CORFO 15IPPID-45676, FONDECYT 1161068), for their financial support. S. Lanfredi thanks FAPESP (grants 2007/03510-9, 2014/11189-0, CNPq and UNESP/PROPe), for their financial support. C.O. Ania thanks the financial support of the Spanish MINECO (grant CTM2011/56770-R).

## Appendix A. Supplementary material

Supplementary data associated with this article can be found, in the online version, at http://dx.doi.org/10.1016/j.jcis.2017.02.028.

## References

[1] R. Andreozzi, V. Caprio, A. Insola, R. Marotta, Advanced oxidation processes (AOP) for water purification and recovery, Catal. Today 53 (1999) 51–55.

[2] J.-M. Herrmann, C. Guillard, P. Pichat, Heterogeneous photocatalysis: an emerging technology for water treatment, Catal. Today 17 (1993) 7–20.
[3] O. Legrini, E. Oliveros, Photochemical processes for water treatment, Chem. Rev. 93 (1993) 671–698.
[4] G. Zhang, J. Gong, X. Zou, F. He, H. Zhang, Q. Zhang, Y. Liu, X. Yang, B. Hu, Photocatalytic degradation of azo dye acid red G by $KNb_3O_8$ and the role of potassium in the photocatalysis, Chem. Eng. J. 123 (2006) 59–64.
[5] G. Zhang, F. He, X. Zou, J. Gong, F. He, H. Zhang, Q. Zhang, Y. Liu, X. Yang, B. Hu, Preparation and photocatalytic property of potassium niobate $K_6Nb_{10.8}O_{30}$, J. Alloys Compd. 425 (2006) 76–80.
[6] G. Zhang, F. He, X. Zou, J. Gong, H. Tu, H. Zhang, Q. Zhang, Y. Liu, Hydrothermal synthesis and photocatalytic property of $KNb_3O_8$ with nanometer leaf-like network, J. Alloys Compd. 427 (2007) 82–86.
[7] B. Tribotté, J.M. Haussonne, $K_2Sr_4Nb_{10}O_{30}$-based dielectric ceramics having the tetragonal tungsten bronze structure and temperature-stable high permittivity, J. Eur. Ceram. Soc. 19 (1999) 1105–1109.
[8] S. Lanfredi, M.A.L. Nobre, M.R. Besse, A.R.F. Lima, G. Palacio, Spectral deconvolution as a tool to understanding Curie-temperature shifting and niobium off-centering phenomenon in ferroelectrics of type niobates, Appl. Math. Sci. 9 (2015) 5839–5869.
[9] N. Wakiya, J.K. Wang, A. Saiki, K. Shinozaki, N. Mizutani, Synthesis and dielectric properties of $Ba_{1-x}R_{2x/3}Nb_2O_6$ (R: rare earth) with tetragonal tungsten bronze structure, J. Eur. Ceram. Soc. 19 (1999) 1071–1075.
[10] T. Mokkelbost, I. Kaus, R. Haugsrud, T. Norby, T. Grande, M.-A. Einarsrud, High-temperature proton-conducting Lanthanum ortho-Niobate-based materials. Part II: Sintering properties and solubility of alkaline earth oxides, J. Am. Ceram. Soc. 91 (2008) 879–886.
[11] S. Lanfredi, C.X. Cardoso, M.A.L. Nobre, Crystallographic properties of $KSr_2Nb_5O_{15}$, Mater. Sci. Eng., B 112 (2004) 139–143.
[12] O. Desponds, R.L. Keiski, G.A. Somorjai, The oxidative dehydrogenation of ethane over molybdenum-vanadium-niobium oxide catalysts: the role of catalyst composition, Catal. Lett. 19 (1993) 17–32.
[13] H.M. Swaan, Y. Li, K. Seshan, J.G. Van Ommen, J.R.H. Ross, The oxidative coupling of methane and the oxidative dehydrogenation of ethane over a niobium promoted lithium doped magnesium oxide catalyst, Catal. Today 16 (1993) 537–546.
[14] M.M. Lin, Selective oxidation of propane to acrylic acid with molecular oxygen, Appl. Catal. A: Gen. 207 (2001) 1–16.
[15] K. Tanabe, S. Okasaki, Various reactions catalyzed by niobium compounds and materials, Appl. Catal. A: Gen. 133 (1995) 191–218.
[16] M. Schmal, D.A.G. Aranda, R.R. Soares, F.B. Noronha, A. Frydman, A study of the promoting effect of noble metal addition on niobia and niobia alumina catalysts, Catal. Today 57 (2000) 169–176.
[17] A.C.B. Dos Santos, P. Grange, A.C. Faro Jr., Effect of support sulphidation on the hydrocracking activity of niobia-supported nickel and molybdenum catalysts, Appl. Catal. A: Gen. 178 (1999) 29–38.
[18] M. Paulis, M. Martín, D.B. Soria, A. Díaz, J.A. Odriozola, M. Montes, Preparation and characterization of niobium oxide for the catalytic aldol condensation of acetone, Appl. Catal. A: Gen. 180 (1999) 411–420.
[19] K. Domen, A. Kudo, A. Tanaka, T. Onishi, Overall photodecomposition of water on a layered niobiate catalyst, Catal. Today 8 (1990) 77–84.
[20] J. Matos, P.S. Poon, S. Lanfredi, M.A.L. Nobre, Functional nanostructured catalysts based on the niobates to the dry methane reforming and ethylene homologation reactions, Fuel 107 (2013) 503–510.
[21] S. Lanfredi, M.A.L. Nobre, P.G.P. Moraes, J. Matos, Photodegradation of phenol red on a Ni-doped niobate/carbon composite, Ceram. Int. 40 (2014) 9525–9534.
[22] A. Houas, H. Lachheb, M. Ksibi, E. Elaloui, C. Guillard, J.-M. Herrmann, Photocatalytic degradation pathway of methylene blue in water, Appl. Catal. B: Environ. 31 (2001) 145–157.
[23] H. Zhang, X.J. Lv, Y.M. Li, Y. Wang, J.H. Li, P25-graphene composite as a high performance photocatalyst, ACS Nano 4 (2010) 380–386.
[24] C. Pelekani, V.L. Snoeyink, Competitive adsorption between atrazine and methylene blue on activated carbon: the importance of pore size distribution, Carbon 38 (2000) 1423–1436.
[25] X. Yan, T. Ohno, K. Nishijima, R. Abe, B. Ohtani, Is methylene blue an appropriate substrate for a photocatalytic activity test? A study with visible-light responsive titania, Chem. Phys. Lett. 429 (2006) 606–610.
[26] M. Inagaki, M. Nonaka, F. Kojin, T. Tsumura, M. Toyoda, Cyclic performance of carbon-coated $TiO_2$ for photocatalytic activity of methylene blue decomposition, Environ. Technol. 27 (8) (2006) 521–528.
[27] J. Matos, A. Garcia, L. Zhao, M.M. Titirici, Solvothermal carbon-doped $TiO_2$ photocatalyst for the enhanced methylene blue degradation under visible light, Appl. Catal. A: Gen. 390 (2010) 175–182.
[28] H.W.P. Carvalho, A.P.L. Batista, P. Hammer, T.C. Ramalho, Photocatalytic degradation of methylene blue by $TiO_2$-Cu thin films: Theoretical and experimental study, J. Hazar. Mater. 184 (2010) 273–280.
[29] J. Matos, M. Rosales, A. García, C. Nieto-Delgado, J.R. Rangel-Mendez, Hybrid photoactive materials from municipal sewage sludge for the photocatalytic degradation of methylene blue, Green Chem. 13 (2011) 3431–3439.
[30] Y.J. Acosta-Silva, R. Nava, V. Hernández-Morales, S.A. Macías-Sánchez, M.L. Gómez-Herrera, B. Pawelec, Methylene blue photodegradation over titania-decorated SBA-15, Appl. Catal. B: Environ. 110 (2011) 108–117.
[31] T.J. Bandosz, J. Matos, M. Seredych, M.S.Z. Islam, R. Alfano, Photoactivity of S-doped nanoporous activated carbons: a new perspective for harvesting solar energy on carbon-based semiconductors, Appl. Catal. A: Gen. 445–446 (2012) 159–165.
[32] S. Lanfredi, D.H.M. Gênova, I.A.O. Brito, A.R.F. Lima, M.A.L. Nobre, Structural characterization and Curie temperature determination of a sodium strontium niobate ferroelectric nanostructured powder, J. Solid State Chem. 184 (2011) 990–1000.
[33] J.R. Carvajal, An Introduction to the Program FullProff 2000, CEA/Saclay, France, 2008.
[34] G. Caglioti, A. Paoletti, F.P. Ricci, Choice of collimators for a crystal spectrometer for neutron diffraction, Nucl. Instrum. 3 (1958) 223–228.
[35] W.S. Rasband, ImageJ, U.S. National Institutes of Health, MD, 1997–2007.
[36] J.B. Parra, C.O. Ania, A. Arenillas, F. Rubiera, J.J. Pis, J.M. Palacios, Structural changes in polyethylene terephthalate (PET) waste materials caused by pyrolysis and $CO_2$ activation, Adsorpt. Sci. Technol. 24 (2006) 439–449.
[37] F. Rouquerol, J. Rouquerol, K.S.W. Sing, P. Llewellyn, G. Maurin, Adsorption by Powders and Porous Solids: Principles, Methodology and Applications, second ed., Elsevier, Oxford, 2014.
[38] P. Kubelka, New contributions to the optics of intensely light-scattering materials, J. Opt. Soc. Am. 38 (1948) (1948) 448–457.
[39] J. Matos, R. Montaña, E. Rivero, Influence of activated carbon upon the photocatalytic degradation of methylene blue under UV–vis irradiation, Environ. Sci. Pollut. Res. 22 (2015) 784–791.
[40] H.E.A. Belghiti, A. Simon, P. Gravereau, A. Villesuzanne, M. Elaatmani, J. Ravez, Ferroelectric and crystallographic properties of the $Sr_{2-x}K_{1+x}Nb_5O_{15-x}F_x$ solid solution, Solid State Sci. 4 (2002) 933–940.
[41] G.K. Williamson, W.H. Hall, X-ray line broadening from filed Al and W, Acta Metall. 1 (1953) 22–31.
[42] M.A.L. Nobre, E.R. Leite, E. Longo, J.A. Varela, Synthesis and sintering of ultra fine $NaNbO_3$ powder by use of polymeric precursors, Mater. Lett. 28 (1996) 215–220.
[43] E.R. Leite, M.A.L. Nobre, E. Longo, J.A. Varela, Particle growth during calcination of polycation oxides synthesized by the polymeric precursors method, J. Am. Ceram. Soc. 80 (1997) 2649–2657.
[44] M. Thommes, K. Kaneko, A.V. Neimark, J.P. Olivier, F. Rodriguez-Reinoso, J. Rouquerol, K.S.W. Sing, Physisorption of gases, with special reference to the evaluation of surface area and pore size distribution (IUPAC Technical Report), Pure Appl. Chem. 87 (2015) 1051–1069.
[45] R.C. Pullar, K. Okeneme, N. McN, Alford, Temperature compensated niobate microwave ceramics with the columbite structure, $M^{2+}Nb_2O_6$, J. Eur. Ceram. Soc. 23 (2003) 2479–2483.
[46] S. Lanfredi, I.A.O. Brito, C. Polini, M.A.L. Nobre, Deriving the magnitude of niobium off-center displacement in ferroelectric niobates from infrared spectroscopy, J. Appl. Spectrosc. 79 (2012) 254–260.
[47] J. Torrent, V. Barrón, Encyclopedia of Surface and Colloidal Science, Marcel Dekker Inc., New York, 2002.
[48] L. Yan, J. Zhang, X. Zhou, X. Wu, J. Lan, Y. Wang, G. Liu, J. Yu, L. Zhi, Crystalline phase-dependent photocatalytic water splitting for hydrogen generation on $KNbO_3$ submicro-crystals, Int. J. Hydrogen Energy 38 (2013) 3554–3561.
[49] G. Zhang, Y. Li, J. Wang, H. Tu, X. Yu, Characterization and photocatalytic activity of $KSr_2Nb_5O_{15}$ with tungsten bronze structure, J. Wuhan Univ. Technol. Mater. Sci. Ed. 24 (2009) 742–746.
[50] J. Matos, J. Laine, J.M. Herrmann, Synergy effect in the photocatalytic degradation of phenol on a suspended mixture of titania and activated carbon, Appl. Catal. B: Environ. 18 (1998) 281–291.
[51] J. Matos, J. Laine, J.M. Herrmann, Effect of the type of activated carbons on the photocatalytic degradation of aqueous organic pollutants by UV-Irradiated titania, J. Catal. 200 (2001) 10–20.
[52] L.G. Chatten, L.E. Harris, Relationship between pKb ($H_2O$) of organic compounds and $E_{1/2}$ values in several nonaqueous solvents, Anal. Chem. 34 (1962) 1495–1501.
[53] T. Cordero, J.-M. Chovelon, C. Duchamp, C. Ferronato, J. Matos, Surface nano-aggregation and photocatalytic activity of $TiO_2$ on H-type activated carbons, Appl. Catal. B: Environ. 73 (2007) 227–235.
[54] C.E.C. Wood, D. Jena (Eds.), Polarization Effects in Semiconductors: From Ab Initio Theory to Device Applications, first ed., Springer-Verlag, NY, United States, 2008.
[55] C. Lubritto, K. Rosciszewski, A.M. Oles, The role of apical oxygen in the high-temperature superconductors, J. Phys.: Condens. Matter 8 (1996) 11053–11068.
[56] J. Matos, A. García, P.S. Poon, Environmental green chemistry applications of nanoporous carbons, J. Mater. Sci. 45 (2010) 4934–4944.
[57] L.F. Velasco, R.J. Carmona, J. Matos, C. Ania, Performance of activated carbons in consecutive phenol photooxidation cycles, Carbon 73 (2014) 206–215.
[58] L. Jing, Y. Xu, S. Huang, M. Xie, M. He, H. Xu, H. Li, Q. Zhang, Novel magnetic $CoFe_2O_4$/Ag/$Ag_3VO_4$ composites: highly efficient visible light photocatalytic and antibacterial activity, Appl. Catal. B: Environ. 199 (2016) 11–22.